9th South African Conference on Computational and Applied Mechanics
Somerset West
14 – 16 January 2014

Numerical evaluation of pulse-echo damage detection in train rail

Craig S. Long*, Philip W. Loveday

CSIR Materials Science and Manufacturing

*clong@csir.co.za

Abstract: A guided wave based monitoring system for welded freight rail, has previously been developed. The existing system was designed to only detect complete breaks. Current research efforts are focused on including a pulse-echo mode of operation in order to detect, locate and possibly monitor damage before a complete break occurs. For this application, it would be advantageous to distinguish between cracks, which could result in rail breaks, and other scattering defects which do not represent damage such as welds. We investigate the interaction between long-range propagating modes and selected weld and crack geometries in an attempt to relate scattering behaviour to defect geometry. Four candidate modes, suitable for long range propagation, are identified and evaluated. A weighted average reflection coefficient is defined and used as a measure to quantify mode conversion between these four modes. The results show that it should be possible to distinguish between a large crack in the crown of the rail and a weld. We also present a procedure to convert reflection and transmission modal amplitudes, computed in the frequency domain, to time domain signals.

Keywords: Rail, damage, Semi-Analytical Finite Element (SAFE), guided waves

INTRODUCTION

One important application of guided elastic waves is that of rail condition monitoring, where significant lengths of rail track can be monitored using permanently installed transmit and receive transducers. This concept has resulted in the joint development of a monitoring system by the Institute for Maritime Technology (IMT) and the Council for Scientific and Industrial Research (CSIR). This Ultrasonic Broken Rail Detection (UBRD) system, consists of alternating transmit and receive stations positioned roughly 1 km apart in a pitch-catch configuration. The system is currently intended to only reliably detect complete breaks without false alarms [1]. Although large defects have occasionally been detected, increasing the sensitivity to these defects results in increased risk of false alarms. The feasibility of adding a pulse-echo mode of operation to this system, while retaining the existing pitch-catch mode (to ensure robustness) is therefore currently being investigated.

There are a number of advantages to adding a pulse-echo capability to the existing system. Examples include the ability to detect and monitor reflections from defects before complete breakage, as well as the ability to locate and possibly even charaterise the damage, based on the time of flight and the characteristics of the propagating modes that are back-scattered from the defect. The authors have recently experimentally demonstrated the feasibility of this concept by detecting reflections from thermite welds up to a distance of over 500m in the field [2, 3].

In this paper, numerical modelling techniques will be used to investigate the complex coupling that occurs when guided elastic waves interact with a discontinuity in a waveguide. Several authors have developed

hybrid techniques suitable for this purpose in recent years [4-6]. As illustrated in Figure 1, these methods use a full 3D model of the volume immediately surrounding the defect (allowing for complex geometries) while modelling the semi-infinite waveguides using Semi-Analytical Finite Element (SAFE) models, thereby reducing computational effort. In particular, we employ the method suggested by Benmeddour et al. [5]. In our previous work [7], we have demonstrated the computation of power reflection coefficients for a rail at operational frequencies of the UBRD system. The aim of this current work is to use this model to quantitatively predict what kinds of damage could be detected using a pulse-echo configuration and also how these characteristics can be distinguished from welds which also act as reflectors.

In a recent contribution [8], candidate modes suitable for long-range operation were identified by the authors, using our experience with elastic wave propagation in train rail. A scalar measure of power reflected from a discontinuity for each incident and reflected mode combination was established. This information was presented graphically in the form of a reflection map for each of the geometries considered, and used to propose combinations of modes potentially capable of distinguishing between reflections from cracks and those from welds. In this paper, we attempt to extend our analysis capability by post-processing the computed modal amplitudes (computed in the frequency domain) to predict time domain signals which could be used to compare with field experiments in future.

We begin by briefly presenting the finite element formulation employed, and criteria used to select the candidate modes for the application. We propose post-processing techniques in both the frequency and the time domains, which could be used in future to conceptualise a suitable pulse-echo configuration. Some preliminary numerical results are offered and concluding remarks presented.

HYBRID SAFE-3D FINITE ELEMENT FORMULATION

In this section, a brief description of the numerical modelling techniques employed will be presented. The implementation is based closely on the hybrid method proposed by Benmeddour et al. [5]. The technique calls for both a semi-analytical finite element (SAFE) and a solid 3-D finite element (FE) implementation.

The SAFE element formulation used in this study is relatively well known, and is based on the implementation of Hayashi et al. [9]. These finite elements are formulated with a complex exponential function to describe the variation of the displacement field along the waveguide, while conventional finite element interpolation functions are employed over the area of the element. This means that only a two-dimensional finite element mesh of the waveguide cross-section is required to model the entire semi-infinite waveguide. For example, in Figure 1 the incoming and out-going semi-infinite waveguides are modeled using the SAFE method, while the arbitrary volume, possibly containing a defect, would be modelled using conventional 3D solid elements.

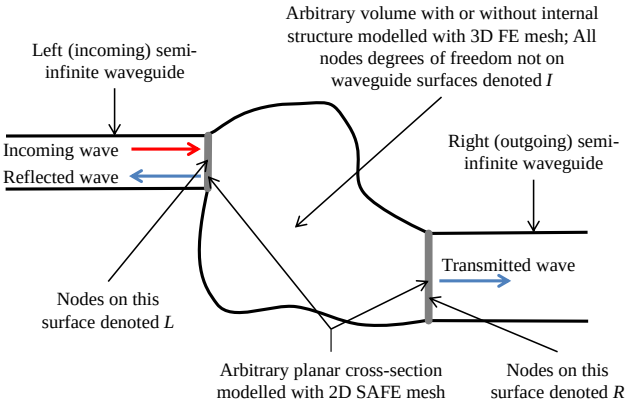

Figure 1 Schematic of arbitrary problem under investigation.)

The displacement fields (u, v, w) in an elastic waveguide, extending in the z direction, can be written as:

$$\begin{aligned} u(x,y,z,t) &= u(x,y)\cdot e^{-j(\kappa z-\omega t)} \\ v(x,y,z,t) &= v(x,y)\cdot e^{-j(\kappa z-\omega t)} \\ w(x,y,z,t) &= w(x,y)\cdot e^{-j(\kappa z-\omega t)} \end{aligned} \quad \ldots (1)$$

where, z is the coordinate in the direction along the waveguide, κ the wavenumber and ω the frequency. Application of conventional finite element interpolation functions over the cross-section results in the system of equations of motion in (2), which has been complemented with an identity so that the solution at a particular frequency may be obtained.

$$\begin{bmatrix} K_0-\omega^2 M & 0 \\ 0 & -K_2 \end{bmatrix}\begin{Bmatrix} u \\ \kappa u \end{Bmatrix}+\kappa\begin{bmatrix} K_1 & K_2 \\ K_2 & 0 \end{bmatrix}\begin{Bmatrix} u \\ \kappa u \end{Bmatrix}=\begin{Bmatrix} 0 \\ 0 \end{Bmatrix} \quad \ldots (2)$$

At a specified frequency the eigenproblem in (2) may be solved to compute the mode shapes and wavenumbers. Real values of wavenumber indicate propagating modes. Imaginary and complex wavenumbers correspond to modes with exponential decay over distance and are required here to satisfy boundary conditions, but they do not transport energy. The solid 3-D finite elements used to model the region with discontinuity are standard displacement based elements, and more detail about their formulation can be found in, for example Cook et al. [10].

A partitioned variational statement is developed by Benmeddour et al. [5] in which the displacements of the arbitrary volume depicted in Figure 1 are divided into degrees of freedom in contact with the left waveguide, denoted L, with the right waveguide, R, and the remaining degrees of freedom in the interior of the volume, I

$$\begin{Bmatrix} \delta\mathbf{U}_L \\ \delta\mathbf{U}_I \\ \delta\mathbf{U}_R \end{Bmatrix}^T\begin{bmatrix} \mathbf{D}_{LL} & \mathbf{D}_{LI} & \mathbf{D}_{LR} \\ \mathbf{D}_{IL} & \mathbf{D}_{II} & \mathbf{D}_{IR} \\ \mathbf{D}_{RL} & \mathbf{D}_{RI} & \mathbf{D}_{RR} \end{bmatrix}\begin{Bmatrix} \mathbf{U}_L \\ \mathbf{U}_I \\ \mathbf{U}_R \end{Bmatrix}-\begin{Bmatrix} \delta\mathbf{U}_L \\ \delta\mathbf{U}_I \\ \delta\mathbf{U}_R \end{Bmatrix}^T\begin{Bmatrix} \mathbf{f}_L \\ \mathbf{0} \\ \mathbf{f}_R \end{Bmatrix}=0, \quad \ldots (3)$$

In these equations, **B** and **T** represents the set of displacement and force modes respectively, calculated from a SAFE eigenvalue analysis and some post-processing to compute **T**. As before, the subscripts L and R denote the left and right waveguides and the + and – superscripts denote forward and backward propagating modes. The direction of propagation is identified based on the sign of the group velocity for real wavenumbers, and the sign of the imaginary part of the wavenumber for evanescent modes. After some manipulation, the following linear system results:

$$\begin{bmatrix} \mathbf{B}_L^{-T} & \mathbf{0} & \mathbf{0} \\ \mathbf{0} & \mathbf{I} & \mathbf{0} \\ \mathbf{0} & \mathbf{0} & \mathbf{B}_R^{+T} \end{bmatrix}\left(\begin{bmatrix} \mathbf{D}_{LL} & \mathbf{D}_{LI} & \mathbf{D}_{LR} \\ \mathbf{D}_{IL} & \mathbf{D}_{II} & \mathbf{D}_{IR} \\ \mathbf{D}_{RL} & \mathbf{D}_{RI} & \mathbf{D}_{RR} \end{bmatrix}\begin{bmatrix} \mathbf{B}_L^- & \mathbf{0} & \mathbf{0} \\ \mathbf{0} & \mathbf{I} & \mathbf{0} \\ \mathbf{0} & \mathbf{0} & \mathbf{B}_R^+ \end{bmatrix}-\begin{bmatrix} \mathbf{T}_L^- & \mathbf{0} & \mathbf{0} \\ \mathbf{0} & \mathbf{0} & \mathbf{0} \\ \mathbf{0} & \mathbf{0} & \mathbf{T}_R^+ \end{bmatrix}\right)\begin{Bmatrix} \boldsymbol{\alpha}_L^- \\ \mathbf{U}_I \\ \boldsymbol{\alpha}_R^+ \end{Bmatrix}=-\begin{bmatrix} \mathbf{B}_L^{-T} & \mathbf{0} & \mathbf{0} \\ \mathbf{0} & \mathbf{I} & \mathbf{0} \\ \mathbf{0} & \mathbf{0} & \mathbf{B}_R^{+T} \end{bmatrix}\left(\begin{bmatrix} \mathbf{D}_{LL} & \mathbf{D}_{LI} & \mathbf{D}_{LR} \\ \mathbf{D}_{IL} & \mathbf{D}_{II} & \mathbf{D}_{IR} \\ \mathbf{D}_{RL} & \mathbf{D}_{RI} & \mathbf{D}_{RR} \end{bmatrix}\begin{bmatrix} \mathbf{B}_L^+ \\ \mathbf{0} \\ \mathbf{0} \end{bmatrix}-\begin{bmatrix} \mathbf{T}_L^+ \\ \mathbf{0} \\ \mathbf{0} \end{bmatrix}\right)\boldsymbol{\alpha}_L^+, \quad \ldots (4)$$

which can be solved for the unknown modal amplitudes of the reflection from the left face, $\boldsymbol{\alpha}_L^-$, the transmitted modal amplitudes through the right surface, $\boldsymbol{\alpha}_R^+$, and the displacements of the interior volume $\mathbf{U}_I$, in terms of known incident modal amplitudes $\boldsymbol{\alpha}_L^+$.

The results of numerical studies are often presented in terms of power and not modal amplitude. Power can be simply computed as in [5]. The reflection and transmission coefficients are then, respectively, computed by dividing the transmitted or reflected power by the power of the incident wave as follows:

$$R_{mn} = \frac{P_{Ln}^{-}}{P_{Lm}^{+}}, \quad T_{mn} = \frac{P_{Rn}^{+}}{P_{Lm}^{+}}. \qquad \text{... (5)}$$

MODE SELECTION

Many propagating modes are excited in the frequency range of operation (25-45 kHz) as can be seen from the dispersion curves, computed using the SAFE method for the relevant rail profile (solved using (2)), depicted in Figure 2(a). However, not all of these modes are suitable for long range propagation. For example, modes with large displacements in the foot of the rail will be strongly attenuated, and highly dispersive modes are also not suitable. Furthermore, the limited placement options for transducers permanently attached to the rail means that only certain modes would be effectively excited.

Four candidate modes were identified as numbered in Figure 2(a) with corresponding mode shapes depicted in Figure 2(b). Modes 1 and 2 are symmetric and anti-symmetric respectively, both with energy concentrated in the crown of the rail. Mode 3 has energy more evenly distributed across the rail cross-section, but with little energy in the foot. Mode 4 is concentrated in the web of the rail.

POST-PROCESSING OF ANALYSIS RESULTS

In this section, two post-processing options are explored for the hybrid SAFE-3D analysis. The first method uses the power reflection coefficient $R_{(i,r)}(\omega)$ of a specific reflected mode number (r) for a given incident mode number (i) at a circular frequency (ω), as given in (5). An example of such a power reflection coefficient curve is depicted in Figure 3(a). It is convenient to represent this curve as a single weighted average value which could be used as a measure to compare the coupling of various incident and reflected modes for different defects. These values may then be used to construct reflection coefficient maps, similar to those presented by Wilcox et al. [11]. This information would be useful when designing the pulse-echo system.

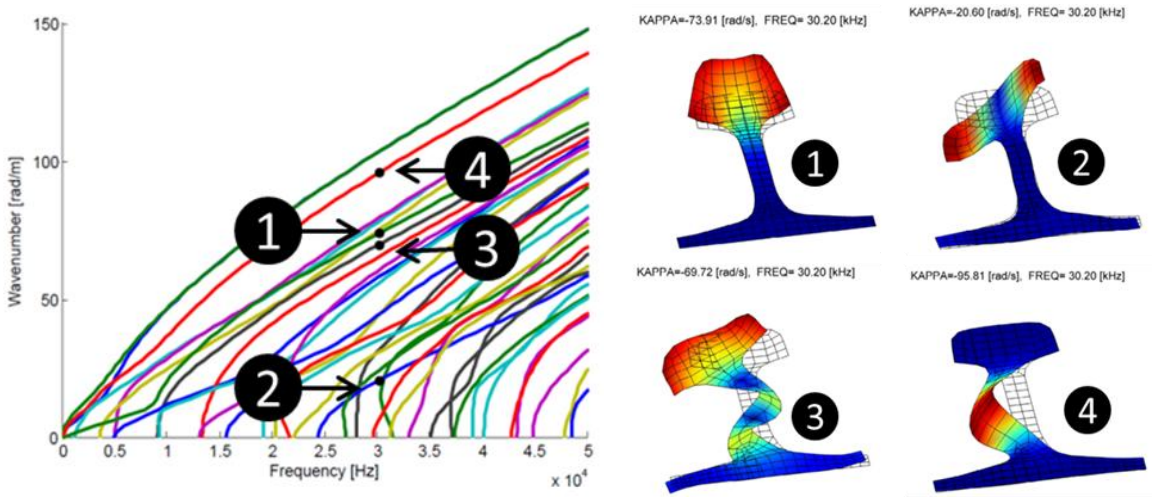

(a) (b)

Figure 2 Candidate modes for long range damage detection using a pulse-echo configuration [8]. (a) Dispersion curves with candidate modes marked and numbered. (b) Mode shapes of candidate modes.

The second method effectively converts the frequency domain data to the time domain. Both the reflected and the transmitted modal amplitudes, $\boldsymbol{\alpha}_L^-(\omega)$ and $\boldsymbol{\alpha}_R^+(\omega)$ respectively, of all modes (real, imaginary and complex) are computed using (4). This information can be exploited to convert a given excitation signal with known frequency content to compute a time-domain response at any distance from the discontinuity. Time domain results are well suited for comparison with experimental data.

Frequency domain post-processing

In order to compute an averaged measure of reflected power, the power spectral density (PSD) of the time dependent incident modal amplitude is selected as a weighting function. A 7.5 cycle Hanning windowed tone burst with unit maximum amplitude and 35 kHz centre frequency is assumed to be a representative driving signal. The PSD for this time signal is depicted in Figure 3(b). This PSD can then be used as a weighting function (or filter) to scale the power reflection coefficient as depicted in Figure 3(c). Finally, this weighted function is integrated over the frequency range of interest, resulting in a scalar measure denoted $\bar{R}_{(i,r)}$, where *i* and *r* represent the incident and reflected mode numbers respectively.

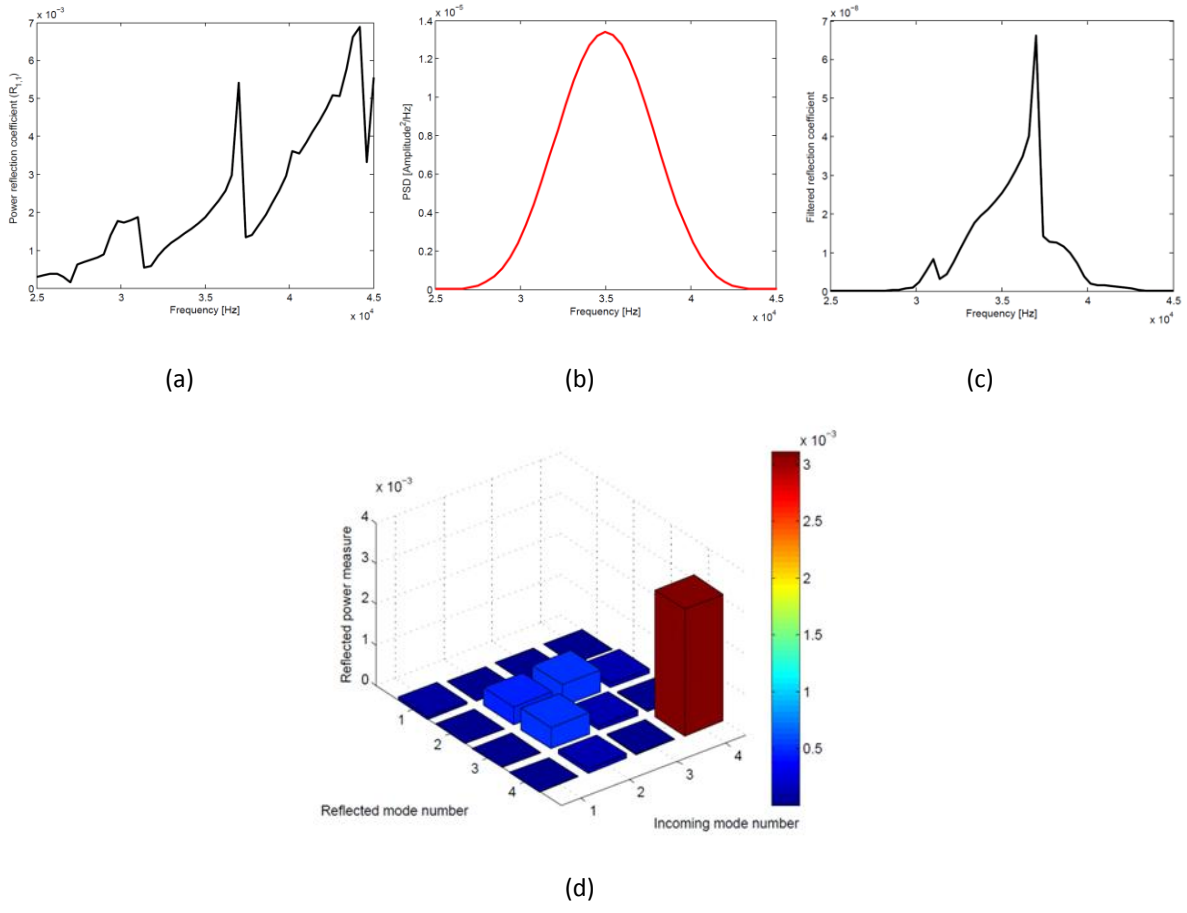

Figure 3 Steps involved in computing the reflection maps [8]. (a) Power reflection coefficient $R_{(i,r)}$ curve for reflected mode (*r*) and incident mode (*i*). (b) PSD used as a weighting function. (c) Power reflection coefficient, weighted by the PSD curve. (d) Reflection map for a thermite weld with a 6mm thick weld cap.

The process is repeated for each incident and reflected mode (with mode numbers as indicated in Figure 2) and the array of scalar values graphically represented as in Figure 3(d). The bar height reflects the magnitude of the reflection measure i.e. the higher the bar, the stronger the reflection. The specific map depicted in Figure 3(d) is for the reflection from a thermite weld with a 6mm thick weld cap as depicted in Figure 4(b). Since the weld cap is ground around the crown of the rail, Modes 1–3 do not reflect as strongly as Mode 4 which has energy concentrated in the web of the rail. Mode 4 is naturally reflected strongest when Mode 4 is incident, i.e. $\bar{R}_{(4,4)}$ is a maximum. These welds are encountered at regular intervals in the field, and we have demonstrated that we are capable of detecting reflections from such a weld at a distance of over 500 m [2]. Therefore, because we would like to estimate how strongly cracks reflect relative to these types of welds, this map will be used as a baseline and can be compare to reflection maps of cracks in order identify differences that could be exploited to differentiate between reflections from a weld and those from a crack.

Time domain post-processing

The computation of the time domain response for a given excitation is fairly straightforward. The frequency content of the time domain excitation signal is given by the Fourier transform of the signal:

$$v(\omega) = \int_{-\infty}^{\infty} v(t) \cdot e^{j\omega t} \mathrm{d}t \quad \text{… (6)}$$

This v(ω) is computed using the Fast Fourier Transform algorithm. The response at distance z is then simply

$$r(z,\omega) = v(\omega) \cdot \sum_{i=1}^{N} \alpha_i(\omega) \boldsymbol{B}_i(\omega) e^{-j\kappa(\omega)z}, \quad \text{… (7)}$$

where $\alpha_i(\omega)$ represents the modal amplitude of either the reflected or transmitted modes and $B_i(\omega)$ are the corresponding mode shapes. Since we are only interested in propagating modes, N represents the number of real wavenumbers. The time-domain response can be computed using the inverse Fourier Transform,

$$v(z,t) = \frac{1}{2\pi} \int_{-\infty}^{\infty} r(z,\omega) \cdot e^{j\omega t} \mathrm{d}\omega, \quad \text{… (8)}$$

which is again computed using the inverse Fast Fourier Transform algorithm.

NUMERICAL RESULTS

This section presents numerical results for selected representative transverse defects in the crown of the rail. Figure 4 depicts the defects considered in this study, including transverse cracks of various sizes (Figure 4(a)) as well as a thermite weld with weld cap as encountered in the field (Figure 4(b)). The results to follow are all generated using 8-noded quadratic SAFE elements and 20-noded hex solid elements.

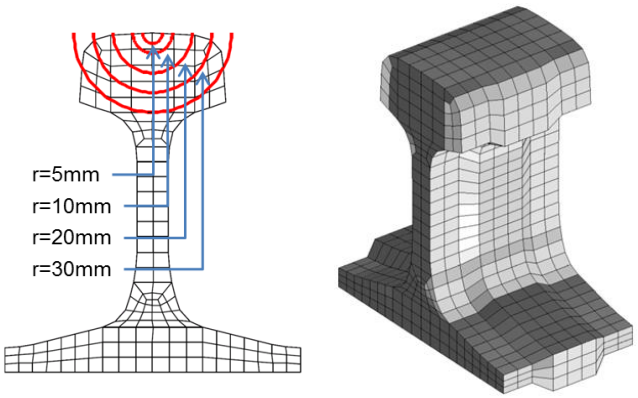

(a) (b)

Figure 4 Defect geometries considered. (a) Cracks of various sizes in the rail crown. (b) Thermite weld with 6mm thick weld cap.

Crown crack size sensitivity

The geometry for this problem is depicted in Figure 4(a), with the concentric arcs representing the edges of circular cracks with radii between 5mm and 30mm. We are particularly interested in this this defect because rail operators report that many complete breaks originate with this crack type. As previously mentioned, we would like to compare maps for this geometry to the reflection map of a regular thermite weld (depicted in Figure 4(b)) in an attempt to find characteristics which could be exploited to distinguish between reflections from welds and cracks. The reflection maps for the crown cracks are depicted in Figures 5(a-d) with independent colour scales, but on the same axis scale as the map for the weld, in order to aid the comparison. The limiting case of no crack, having zero reflection, is not shown here for brevity.

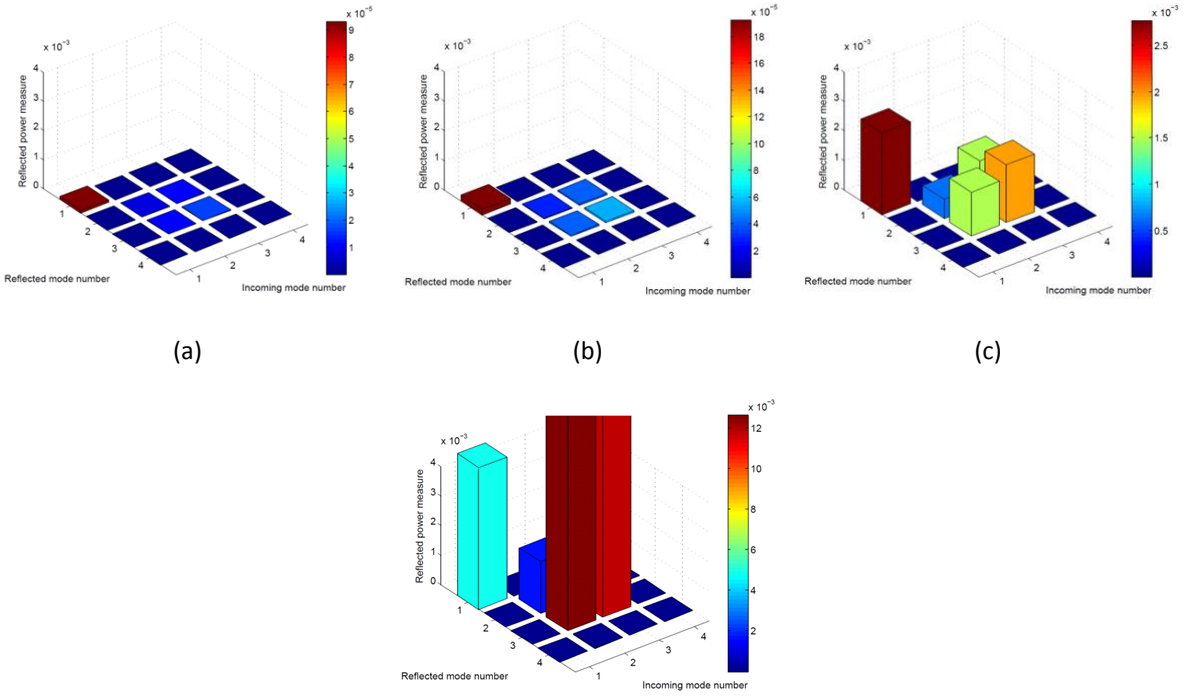

(a) (b) (c)

(d)

Figure 5 Reflection maps for different size circular cracks in the crown, with crack radii of (a) 5mm, (b) 10mm, (c) 20mm and (d) 30mm, respectively as depicted in Figure 4(a) [8].

Similar to the case for the weld, since the crack geometry is symmetric no coupling between symmetric and anti-symmetric modes ($\bar{R}_{(1,2-4)} = \bar{R}_{(2-4,1)} = 0$) is observed. There are however, significant differences in the values of $\bar{R}_{(1,1)}$ and $\bar{R}_{(4,4)}$ when comparing the reflection map of the weld to the maps of the cracks. The crack in the crown has a comparatively negligible value of $\bar{R}_{(4,4)}$, whereas the value of $\bar{R}_{(1,1)}$ grows steadily as the size of the crack increases. For the 5mm crack, the value of $\bar{R}_{(1,1)}$ is 1.5 times greater than that for a thermite weld, while the 10mm crack is 3.2 times, the 20mm crack 46 times and the 30mm crack 79 times larger. We therefore believe that if both Modes 1 and 4 are transmitted and sensed, it will be possible to distinguish between welds and cracks in the crown, using $\bar{R}_{(4,4)}$ to identify welds and $\bar{R}_{(1,1)}$ to identify cracks in the crown.

Finally, the procedure to convert the results to the frequency domain for a given excitation signal is employed to predict the time domain response that could be expected from a 20mm crack in the crown as depicted in Figure 4(a). As before, Mode 1 is excited with a 7.5 cycle Hanning windowed tone burst with unit maximum modal amplitude and 35 kHz centre frequency. The vertical response at the top of the crown is computed. Figure 5(c) illustrates the response is completely dominated by Mode 1 if Mode 1 is used as the incident mode. When reconstructing the time signal, only Mode 1 is therefore used in this case.

The result of this analysis is depicted in Figure 6, with the reflected response measured at 0m, -3m and -6m from the crack respectively. The time taken to propagate can be seen to correspond well with the group velocity of this mode (approximately 3000m/s at 35 kHz). The response has a spurious low amplitude signal which we cannot yet explain.

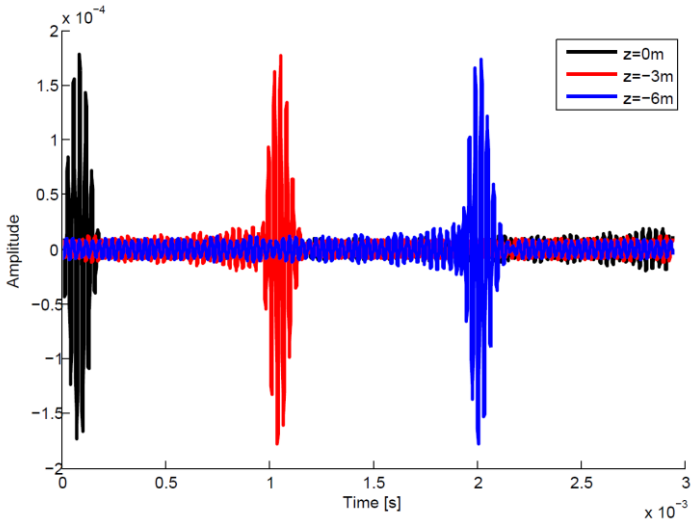

Figure 6 Time domain reflection of Mode 1 with Mode 1 incident measured at 0m, 3m and 6m from the crack.

CONCLUSION

This study forms part of our ongoing effort to extend the existing ultrasonic broken rail detection (UBRD) system by including a pulse-echo mode of operation in order to detect, locate, monitor and possibly characterise damage, before a complete break occurs. We have applied a hybrid SAFE–3D FE method to study the interaction of guided waves with defects in rails. A weighted average scalar measure was defined based on the frequency–dependent power reflection coefficient and the power spectral density of the input

signal. This scalar value has been used to graphically depict, in the form of reflection maps, modes which are likely to reflect strongly for a given incident mode.

Four candidate modes which we believe are capable of transmitting long distance have been identified. We have shown that employing the symmetric mode with energy concentrated in the crown of the rail (denoted Mode 1 in this study) and the mode with energy concentrated in the web (Mode 4), it should be possible to distinguish between cracks in the crown and thermite welds. We have also presented a post-processing procedure to convert the frequency domain result to the time domain for future comparison with experimental data or explicit time-domain simulations. This procedure still contains a small spurious error signal which will be further investigated in future.

ACKNOWLEDGMENTS

Funding for this project, provided by CSIR, the Department of Science and Technology and the National Research Foundation of South Africa (Grant No's: 78858 and 85330), is gratefully acknowledged.

REFERENCES

1 F. A. Burger, "A practical continuous operating rail break detection system using guided waves", in Proc. *18th World Conference on Nondestructive Testing*, Durban, South Africa, Paper no. 627 (April 2012).

2 P. W. Loveday and C. S. Long, "Long range guided wave defect monitoring in rail track", to appear in Review of Progress in Quantitative Nondestructive Evaluation, (2013).

3 P. W. Loveday and C. S. Long, "Feasibility of detecting cracks in rail track at long range using guided wave ultrasound", to appear in Proc. *9th South African Conference on Computational and Applied Mechanics*, (2014).

4 Y. N. Al-Nassar, S. K. Datta, and A. H. Shah, "Scattering of Lamb waves by a normal rectangular strip weldment", *Ultrasonics*, **29**, pp. 125-132 (1991).

5 F. Benmeddour, F. Treyssède, and L. Laguerre, "Numerical modeling of guided wave interaction with non-axisymmetric cracks in elastic cylinders", *International Journal of Solids and Structures*, **48**(5), pp. 764-774 (2011).

6 V. Baronian, A. Lhémery, and A.-S. Bonnet-BenDhia, "Simulation of non-destructive inspections and acoustic emission measurements involving guided waves", *Journal of Physics: Conference Series*, **195** 012001 (2009).

7 C. S. Long and P. W. Loveday, "Analysis of guided wave scattering due to defects in rails using a hybrid FE-SAFE method", in *Review of Progress in QNDE*, 32A, edited by D. O. Thomson and D. E. Chimenti, AIP Conference Proceedings vol. 1511, American Institute of Physics, Melville, NY (2013), pp. 238–245.

8 C.S. Long and P.W. Loveday, "Prediction of guided wave scattering by defects in rails using numerical modelling", to appear in Review of Progress in Quantitative Nondestructive Evaluation, (2013).

9 T. Hayashi, W.-J. Song, and J. L. Rose, "Guided wave dispersion curves for a bar with an arbitrary cross-section, a rod and rail example," *Ultrasonics*, vol. 41, no. 3, pp. 175-183, (May 2003).

10 R. D.Cook, D. S. Malkus, M. E. Plesha and R. J. Witt, "Concepts and Applications of Finite Element Analysis, 4th Edition", John Wiley & Sons, (2002).

11 P. Wilcox, M. Evans, B. Pavlakovic, D. Alleyne, K. Vine, P. Cawley and M. Lowe, "Guided wave testing of rail", *Insight-Non-Destructive Testing and Condition Monitoring*, **45**(6), 413-420 (2003).